Effect of minor quantities of Ca, Al, and Mg on reaction kinetics, porosity and strength of Fe-rich alkali-activated fayalitic slag

Nana Wen[a,b], Arne Peys[c], Tobias Hertel[a], Yiannis Pontikes[a]

[a] KU Leuven Department of Materials Engineering, Sustainable Resources for Engineered Materials (SREMat), Kasteelpark Arenberg 44, 3001 Leuven, Belgium

[b] SIM vzw, Technologiepark 935, BE-9052 Zwijnaarde, Belgium

[c] Sustainable Materials, VITO, Boeretang 200, 2400, Mol, Belgium

Abstract

Alkali-activated materials can be formed by alkali-activation of Fe-rich non-ferrous metallurgy slags (AA-NFMS). To study NFMS in AA-NFMS systematically, five NFMS were synthesized, with different CaO (6-16 wt%), Al_2O_3 (7-11 wt%) and MgO (0-4 wt%) contents, while keeping the same FeO_x/SiO_2 molar ratio. The effect of slag chemistry and the alkali ions (Na^+/ K^+ = 0, 0.5 and 1) in alkali-activating solution on the reaction kinetics, compressive strength (3, 7 and 28 days), and pore structure of AA-NFMS, were investigated. The reactivity up to 3 days was evaluated via isothermal calorimetry, and the pore structure was measured via mercury intrusion porosimetry. Higher Al/Si in the slag showed higher reactivity, higher compressive strength and lower total porosity of the AA-NFMS. Higher Ca/Si yielded lower cumulative heat after 3 days and decreased early compressive strength but higher strength after 28 days of curing. Ca replacement by Mg lead to faster reaction kinetics but inferior mechanical properties and increased porosity. Increased K^+ concentration in activator resulted in higher reactivity and compressive strength despite the higher total porosity. Empirical model fitting using JMP software revealed that $K^+/(N^+{+}K^+)$ in the activator, Ca/Si, and (Ca+Mg)/Si in NFMS are significant factors that affect the strength of AA-NFMS.

Keywords: Fe-rich slag, alkali-activated material, reaction kinetics, porosity, compressive strength

1. Introduction

Considering the known issues associated with Portland cement production, such as greenhouse gas emissions, non-renewable resources and energy consumption [1], sustainable alternative binders, like alkali-activated materials (AAM) received a boost of interest over the last years [2-6]. The environmental footprint of AAMs has on many occasions come out positively in comparative life cycle assessment calculations with Portland cement (PC) [7-10]. Especially, in light of the strive for climate neutrality in the near future, avoiding the need to decarbonate limestone and clinkering at ~1450 °C to produce PC is a large environmental benefit for AAM. Not only the smaller environmental footprint but also excellent physical, mechanical, and thermal properties make AAM an active research area [4, 11-13]. AAM are typically produced as a result of the reaction of a solid silicate precursor (e.g., slag, fly ash and metakaolin) with an alkaline solution (e.g. alkali silicate, alkali hydroxide solutions). The wide range of precursors that can be used is an additional benefit of the AAM, as this presents a valuable route to valorize mineral residues, which are otherwise not easily applied in construction materials, such as biomass ashes, mine tailings, waste glass, ceramic residues, catalyst residues, incinerated sludge and slags from the non-ferrous metallurgy [13-15].

Despite a large number of research papers on slag-based AAMs, the studied slag is almost exclusively blast furnace slag (BFS) from the production of iron [16] and there is much less attention on slags from non-ferrous metallurgy. Non-ferrous metallurgy slags (NFMS) predominantly result from the processing of copper, nickel, phosphorus lead and zinc [17]. Among these, NFMS from copper production, which has undergone the most extensive research work, typically contains high-Fe and low-Ca, and often contains heavy metals, thereby

presenting a leaching risk if not properly treated [17, 18]. In some countries, NFMS is therefore still landfilled or finds applications with relatively low added value [19]. This is fortunately not the case for NFMS in general. In the selected plants worldwide, metals are more efficiently extracted resulting in (next to larger metal yields) a clean NFMS, which can reach the environmental compliance for construction materials imposed by local legislation. As an example, consider the copper slag produced by Aurubis Beerse in Belgium. The results of leaching analysis conducted via column tests revealed that the leaching of all elements remains well below the prescribed limits [20].

The amorphous nature of NFMS makes the most of its reactivity and thus favors the alkali activation process [21, 22]. It has previously been observed [23] that the reactivity of NFMS is highly related to the cooling speed at the end of slag production. The authors [23] investigated three different methods for slag quenching and noticed that a higher cooling rate promotes the reactivity of the slag due to a higher amount of amorphous phase, while a slow cooling method led to the formation of more crystalline phases, such as fayalite and magnetite, and thus a lower reactivity. However, the reactivity of NFMS even with a fully amorphous phase is still lower compared to commonly used precursors like BFS. In a study conducted by Stefanini et al. [24], they substituted BFS with NFMS and observed that this substitution slowed down the reaction kinetics. It also resulted in a slight increase in porosity (approximately 2% when fully replaced) and a reduction in compressive strength. However, over time, the disparities in these properties became less pronounced. Apart from the lower reactivity of NFMS, what makes the study of NFMS into AAM rather complex is the notable difference in NFMS chemistry from source to source and also the multiple oxidation states of Fe (Fe^{2+}, Fe^{3+}) in NFMS [23]. To gain a deep insight into the alkali-activated NFMS (AA-NFMS) system, Siakati et. al [25] started with binary (FeO_x-SiO_2) synthetic slags and Van De Sande et. al [15] continued with ternary (FeO_x-SiO_2-CaO) synthetic slags. The authors found the incorporation of Ca can significantly affect

the reactivity of the slags and the CaO content in the ternary (FeO_x-SiO_2-CaO) system had a significant effect on the compressive strength [15]. Higher CaO content in the slag resulted in a lower compressive strength at the early age (3 days), but slag with moderate CaO content (12 wt%) obtained the highest strength at the late age (28 days), indicating there is an optimum in terms of chemistry. Furthermore, Peys et. al [26] revealed the alkali activation of NFMS is quite distinct from other AAM systems. Due to the presence of a high concentration of Fe, there are two possible reaction products formed. One is the Fe^{2+} containing structure, in which Fe^{2+} is arranged in a trioctahedral brucite-like layered configuration [26], most likely connected to silica in a similar way as phyllosilicates [27]. The other reaction product is an Fe^{3+} containing structure, in which the Fe^{3+} is similar to Al^{3+} arranged in a silicate polymeric network [26, 28]. Furthermore, AA-NFMS has demonstrated superior fire resistance [29], withstanding temperatures of up to 1000 °C, surpassing traditional cement. Notably, NFMS has found applications beyond AAM, as it has been successfully utilized as supplementary cementitious material (SCM), replacing up to 70% of cement in blended cement formulations [30, 31]. A distinctive hydration product, a (Fe(II), Mg(II))-Al(III))-layered double hydroxide, was identified, a feature not previously observed in other blended cements. Astoveza et al. [32] investigated the incorporation of NFMS into ternary binders containing Portland cement, aluminate cement, and calcium sulfate. They observed that this addition enhanced the dimensional stability of expansive binders, and the Fe from NFMS incorporated in the intermixed hydrate gel phase. The work in the area of NFMS also expands to other metallurgical residue, such as bauxite residue [33, 34], non-ferrous incineration bottom ash [35].

To the best of our knowledge, only binary and ternary synthetic slag systems have been investigated and the existing studies have not dealt with a NFMS system that is closer to real life. According to a recent review [3], the composition of NFMS is dominated by FeO (around

40-60 wt%) and SiO_2 (22-35 wt%) with low levels of Al_2O_3 (2-13 wt%), CaO (0.5-20%) and MgO (0-11 wt%). To provide further insight, it would be therefore interesting to also involve a quaternary system (FeO_x-Al_2O_3-SiO_2-CaO) or an even more comprehensive quinary system with the addition of MgO. A previous study [36] has found that MgO content of synthetic alkali-activated CaO-MgO-Na_2O-Al_2O_3-SiO_2 material can strongly affect C-(N)-A-S-H gel chemistry and nanostructure. Giels et. al [37] tried to add MgO (0, 1, 3 and 5%) in their Fe-rich residue and found the increasing amount of MgO increased Al-bearing spinels and decreased amorphous phase, leading to a decreased compressive strength. Furthermore, other researchers [38, 39] attempted to evaluate the impact of MgO in BFS, and verified that MgO content plays an important role in the reaction products and the pore size distribution of AAM.

The pore structure is arguably the most significant component of cementitious materials regarding strength, permeability and durability [40]. Previous works [41, 42] confirmed that the pore size distribution is highly dependent on both the chemical composition of the precursors and the alkali-activating solutions. Activating solutions usually include sodium and/or potassium hydroxides or combinations of sodium/potassium silicate, sulfates [43] or carbonate [44]. A study [45] on alkali-activated BFS explored different activation solutions, such as NaOH, Na_2SiO_3, Na_2CO_3, and Na_2SO_4, and observed that the slag exhibited a more extensive reaction when activated with NaOH and Na_2SiO_3 solutions. The chemical composition of silicate solution can be defined by the SiO_2/M_2O (M= Na or/and K) molar ratio and the H_2O content. The high alkalinity in activating solution is important for the dissolution and reaction of the precursors [46]. Duxson et al. [47] showed that the increasing ionic size of the elements in the activator results in decreasing pore size and increasing porosity. Steins et. al [41] evaluated two alkali activators (Na^+, K^+) at room temperature using nitrogen sorption and X-ray neutron scattering. The results suggested that the K-activated samples had a greater specific surface area and presented much faster kinetics in the six months of observation.

However, the alkali activation of NFMS with Na-silicate and K-silicate under different slag chemistry has not been well studied, especially a mixture of (Na+K)-silicate is rarely described in the literature. Typically, K-activation has a higher reactivity and compressive strength than its Na-activation counterpart, but also a higher cost and environmental impact. Given the information provided, a mixture (Na+K) activator would be interesting for both scientific and practical aspects.

Considering the above, five synthetic slags in the system FeO_x-SiO_2-Al_2O_3-CaO-MgO were produced keeping the same molar ratio of FeO_x/SiO_2 but varying the molar ratio of CaO/SiO_2 (to 0.6, 0.3 and 0.2), Al_2O_3/SiO_2 (to 0.2 and 0.1) and MgO/SiO_2 (to 0 and 0.2). AA-NFMS was synthesized using three types of silicate activators (Na^+, K^+, or a mixture of Na^++K^+ at a Na/K molar ratio of 1:1). The objective of this study is to provide a comprehensive analysis of the interplay between the composition of the slag, the activating solution, and other properties such as reactivity, mechanical strength, and porosity of AA-NFMS. The novelty of this research lies in the utilization of Fe-rich slag, a material previously considered unsuitable for cementitious applications, and its potential to expand the usage of NFMS. The kinetics of slag reactions are assessed using isothermal calorimetry. The impact of NFMS chemistry on the porosity of AA-NFMS is explored through mercury intrusion porosimetry testing. The interaction of all these factors, including NFMS and activating solution chemistry, on mechanical strength is further examined using custom-designed modules in JMP Pro 14.0.0 software. The control of the pore structure of AA-NFMS is crucial in understanding potential differences in binder durability, a topic currently being pursued in another work. This research, by delving into the specific characteristics of AA-NFMS, is laying the groundwork for the responsible and innovative use of NFMS in AAM, enhancing the sustainability and versatility of cementitious materials in the construction industry. Furthermore, given the significant

variability in industrial slag chemistry, the findings presented here can reveal trends and enable the prediction of AAM performance from a new industrial NFMS with reasonable accuracy.

2. Materials and methods

2.1 Slag synthesis and characterization

Five different NFMS were synthesized with a chemical composition resembling industrial NFMS from copper production. They are named by the molar ratio of each oxide after normalizing to 1 mol of SiO_2, where C represents CaO, A represents Al_2O_3 and M represents MgO (see Table 1). There are three different metal oxides selected as the variables: CaO, Al_2O_3 and MgO. The CaO weight content in C_6A_1, C_3A_1 and C_2A_1 slags is 16%, 10% and 5%, respectively. C_6A_2 has higher Al_2O_3 content (11 wt%) than C_6A_1 (7 wt%) under the same CaO content. To investigate the effect of MgO, 4 wt% CaO in C_3A_1 was replaced by MgO to obtain $C_2A_1M_2$. For the sake of better comparison among slags, the Al_2O_3/SiO_2, Ca/Si and (Ca+Mg)/Si molar ratios are also presented in Table 1.

Table 1 Chemical composition from XRF in mol% (any deviation from 100% is due to rounding errors)

	FeO	SiO_2	CaO	Al_2O_3	MgO	Formula of slag	Al_2O_3/SiO_2	Ca/Si	(Ca+Mg)/Si
C_6A_2	40	33	20	7	0	$F_{1.2}SC_{0.6}A_{0.2}$	0.2	0.6	0.6
C_6A_1	41	35	19	5	0	$F_{1.2}SC_{0.6}A_{0.1}$	0.1	0.6	0.6
C_3A_1	45	38	12	5	0	$F_{1.2}SC_{0.3}A_{0.1}$	0.1	0.3	0.3
C_2A_1	48	39	8	5	0	$F_{1.2}SC_{0.2}A_{0.1}$	0.1	0.2	0.2
$C_2A_1M_2$	44	37	8	5	7	$F_{1.2}SC_{0.2}A_{0.1}M_{0.2}$	0.1	0.2	0.4

The slags were synthesized by a mixture of metallic iron (purity > 99.0 wt%, Höganas) and metal oxides (iron (III) oxide, quartz, magnesium oxide and calcium oxide, purity >99.0 wt%, Sigma-Aldrich) in an iron crucible using an induction furnace (Indutherm TF4000). The mixture was kept for 30 min at 1250 ± 20 °C to ensure homogeneous melting of the pure

powders. This temperature was calculated by FactSage and estimated to be sufficient based on previous work on Fe-rich NFMS [15, 48]. After the 20-minute dwell time, the melt was bubbled with a mixture of CO/CO_2 gas ($CO/CO_2 = 2$), and the molten slag was then quenched in water in order to maximize the amount of amorphous phase. Subsequently, the slag granules were dried in an oven at 110 °C for 24 h to remove the residual moisture. The granules were then crushed in a disc mill (Fritsch Pulverisette 13) and milled using an attritor ball mill (Wiener 1S). The process of activation and the dissolution of the slags depend mainly on the amount and chemistry of the phases present [23] and the fineness of the slag [38]. Thus, to avoid the influence of the fineness on the results and focus on the compositional aspect, the slags were all ground to a similar specific surface area of about 4000 ± 200 cm^2/g, measured according to the air permeability (Blaine) method, EN 196-6.

Wavelength dispersive X-ray fluorescence (XRF, Bruker S8 Tiger 4) was used to measure the chemical composition of the slags using glass bead samples made with 1:10 sample-to-flux ratios. The mineralogical composition after milling was analyzed by a D2 Phaser diffractometer (Bruker) XRD, using Cu Kα radiation of 30 kV and 10 mA with a step size of 0.02 ° and a step time of 0.6 s in a range of 10-70 °2θ. Mineralogical identification was carried out using the software DiffracEVA V4.1.1 (Bruker).

The study on the oxidation state of Fe of the slag is necessary and important since Fe^{2+}/Fe^{3+} is correlated with the polymerization of the molten slag [49]. This is expected to affect dissolution, most likely heat release and also the reaction products forming. The oxidation state of Fe was determined by wet chemical analysis as described in [15]. From this experiment, the total Fe^{2+} content is obtained and the relative proportions of Fe^{2+} and Fe^{3+} can be calculated based on the total FeO amount from the XRF result. Each test was carried out in duplicate.

2.2 Solution preparation

Three alkali activating solutions were used and were prepared by mixing deionized water, sodium hydroxide pellets (>99 wt% purity, Sigma-Aldrich) and/or potassium hydroxide pellets (>85 % purity, Honeywell, Belgium) with commercial sodium silicate with molar ratio SiO_2/Na_2O of 3.3 and 63.5 wt% H_2O (Silmaco, Belgium) or commercial potassium silicate (Silmaco, Belgium) with molar ratio SiO_2/K_2O of 2.85 and 60 wt% H_2O. The final compositions of the activator had a $SiO_2/(Na_2O+K_2O)$ molar ratio of 1.65 and a water content of 65%. The molar ratio $SiO_2/(Na_2O+K_2O)$ is an important parameter for AAM synthesis. When it is lower than 1.6, the solution is regarded as corrosive, otherwise, it will be irritant. A molar ratio of 1.65 was thus selected, considering the previous data where compressive strength at 28 days was quite similar as the molar ratio ranged from 1.6 and 2.0 [50]. The details of the three activators are summarized in Table 2. All solutions were prepared at least one day before the AAM preparation.

Table 2 Detailed information on alkali activating solutions

Activator ID	$\frac{K^+}{K^+ + Na^+}$ $(molar\ ratios)$	Molar ratio $SiO_2/(Na_2O+K_2O)$	Water content (wt%)	pH
N	0	1.65	65	13.59
NK	0.5	1.65	65	13.64
K	1	1.65	65	13.97

2.3 Preparation and characterization of the AA-NFMS

2.3.1 Sample preparation

To perform the test of water absorption, and mercury intrusion porosimetry (MIP) test, cubic (20×20×20 mm^3) paste samples were made. To do so, slag was mixed with the alkali activating solution at a fixed liquid solution to slag mass ratio of 0.4 for 3 min using a hand mixer. In the preparation of AA-NFMS mortar for the compressive test, all formulations were produced with a standard sand/slag mass ratio of 3, and a liquid to slag mass ratio of 0.5, mixed

according to EN 196-1. However, instead of casting into 40×40×160 mm^3 mold as specified in EN 196-1, 20×20×80 mm^3 molds were used due to the relatively low amount of synthetic slag available. After casting, the samples were sealed and placed in an ambient curing room (20 °C, 50% relative humidity) for 24 h. Subsequently, the samples were demolded and remained sealed, under the same condition, until the compressive strength test at 3 days, 7 days and 28 days. Cubic paste samples were cured under the same condition as AAM mortar.

2.3.2 Characterization of the AA-NFMS

2.3.2.1 Reactivity test

The reactivity of the slags under different activators was assessed through isothermal calorimetry for the first 3 days. About 3 g of slag and 1.2 g of alkali activating solution were used for isothermal calorimetry measurements (TAM Air, TA Instruments) at 20 °C. To monitor the reaction kinetics from the very beginning, admix ampoules were used. The solution was injected and the paste was mixed in the ampoule for 2 min.

2.3.2.2 Pore structure analysis

Before the samples were subjected to MIP tests, they were broken into small fragments and subjected to solvent exchange drying to ensure that all pore water was removed. Although the MIP method can give a misleading pore size distribution by overestimating the small pores and underestimating the big pores because of the ink-bottle effect [51], it is still a powerful tool providing insights related to pores size, especially when used for comparative studies. MIP was conducted on a Micrometrics Poresizer 9310. Only the data of pore diameters from 10 nm to 10,000 nm are reported, because it is impossible to differentiate macropores from interparticle space-filling [42].

2.3.2.3 Compressive strength

The flexural and compressive strength tests were carried out on two prismatic mortar specimens (20 × 20 × 80 mm^3) from each mixture with an Instron 5985 testing device at a

displacement rate of 2 mm/m. The present work focuses on compressive strength; the flexural strength was 5.5 ± 1 MPa at 28d for all samples.

2.3.2.4 Microstructure

Microstructure identification was carried out using Electron Probe Microanalysis (EPMA) with a Jeol JXA-8530F instrument equipped with Wavelength Dispersive Spectrometers (WDS) at a beam current of 50 nA and voltage of 20kV. The EPMA sample preparation process involved embedding the samples in Epofix resin, followed by grinding with silicon carbide papers and polishing using diamond suspension. Subsequently, a 2 nm-thick platinum coating was applied to the polished specimens. Various standards were used for the analysis of different elements: Al and Si were quantified using Almandina garnet ($Fe_3Al_2Si_3O_{12}$), Mg with Olivine ($(Mg, Fe)_2SiO_4$), Na and Ca using Plagioclase ($(Na,Ca)Al(Al, Si)Si_2O_8$), and Fe content was determined using Hematite (Fe_2O_3).

2.3.3 JMP model

Empirical model fitted using JMP (Pro 14.0.0) software, a user-friendly statistical analysis tool, to analyze the impact of chemical composition of NFMS and activating solution on the compressive strength development. Key factors such as Ca/Si, Al/Si, (Mg+Ca)/Si, and $K^+/(N^+ + K^+)$ were included in the model, along with their first-order interaction, to determine their relative influence. The software allowed us to explore the relationships between these factors and the outcomes of our experiments, helping us gain valuable insights into the key variables that affect the properties of the materials under study.

3 Results and discussion

3.1 Slag characterization

The five slags had a Blaine specific surface area of 4000 ± 200 cm^2/g (Table 3). The calculated proportion of Fe^{2+}/total Fe is also shown in Table 3. Slags with different CaO

concentrations and Al_2O_3 levels have a similar percentage of Fe^{2+} of around 86.5 ± 0.5 % and Fe^{3+} of 13.5 ± 0.5 %. This is not in line with the trend observed earlier [15], where a higher CaO content in the slag resulted in a higher content of Fe^{3+}. The differences in the results could be possibly attributed to the different slag chemistry. However, the presence of Mg^{2+} made a significant difference in the oxidation state. The addition of MgO decreases the Fe^{2+} and thus increases Fe^{3+} fraction. One possible reason could be that the role of Fe^{2+} is similar to the role of Mg^{2+}. However, this assumption needs to be further proved by analyzing different Mg/Fe to confirm if (Fe^{2+}+Mg^{2+})/total Fe ratio is the same. It was previously discussed that Fe^{2+} plays a network modifying role [14], and the reactivity of Fe^{3+}-rich slags is much lower than Fe^{2+}-rich slags for precursors in an alkali environment [52]. Thus the difference in the reactivity of the investigated slags without the presence of Mg ($C_2A_1M_2$ slag) should not be related to the Fe oxidation state of the slag as that is comparable.

Table 3 Physical properties of the slags

	C_6A_2	C_6A_1	C_3A_1	C_2A_1	$C_2A_1M_2$
Blaine surface area (cm^2/g)	3900	4200	4000	4200	4200
Fe^{2+}/total Fe	0.86	0.87	0.87	0.87	0.80

XRD patterns (see Fig. 1) of the slags show that they are mainly glassy (>98 %) with very little crystalline inclusions of quartz, fayalite or forsterite and maghemite, which indicate the slags were quenched better and/or had a better glass-forming ability compared to previous ternary slag system [15].

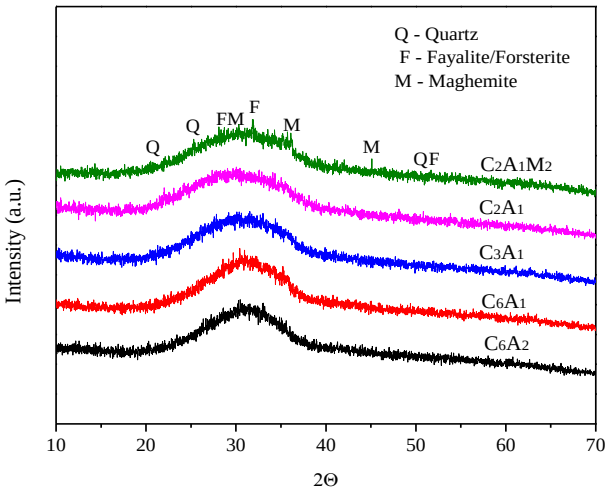

Fig. 1. XRD pattern of the slags produced

3.2 Alkali-activated material

3.2.1 Isothermal Calorimetry

The heat flow in the first 72 h after mixing for five different slags activated by three solutions is shown in Fig. 2. Two peaks are observed in the heat flow curves of all samples, although only the second peak can easily be distinguished. The first exothermic peak appears immediately after mixing, corresponding to the influence of the manual stirring and instant sorption of the activating solution on the surface of slag powder and (partial) dissolution of the slag grains [53]. The second heat flow peak corresponds to the main dissolution and the formation of reaction products [54], and occurs within 2 h for all studied samples. The main heat peak of the AA-C_6A_2, the slag with the highest amount of CaO and Al_2O_3, occurred first and showed the highest heat flow. A comparison among the AA-C_6A_1, C_3A_1 and C_2A_1 shows that with a higher CaO content, the main reaction peak appeared earlier and also with higher intensity. For example, the main peak is at 0.67 h, 1.1 h and 1.39 h for C_6A_1, C_3A_1 and C_2A_1, respectively, using the Na-activator (Fig. 2a), indicating that higher CaO concentration accelerates the kinetics of reaction [55]. From the comparison of C_3A_1 and $C_2A_1M_2$, slag $C_2A_1M_2$ reacted faster and the peak was higher, independent of the choice of alkali activating

solution, suggesting the replacement of CaO by MgO results in faster reaction kinetics in an AAM system. This agrees well with [53], where the higher MgO content was found to result in a faster reaction.

The curves of the cumulative heat release for the five slags and the three activators employed in Fig. 2, provide at first glance a similar view, e.g., most of the heat was released during the first day. The heat release of the AA-C_6A_2 slag is the highest among all five slags after 72 h, independently of the activating solution, followed by $C_2A_1M_2$, C_2A_1 or C_3A_1, and C_6A_1. Interestingly, C_6A_1 had the lowest cumulative heat release at the end, even though the AA-C_6A_1 had faster reaction kinetics than the middle and lower CaO content AA-NFMS system based on the heat flow curves. The difference in total cumulative heat among these three systems was higher when K-silicate was used as the activator. AA-$C_2A_1M_2$ in all cases first reached a heat flow plateau. The slope of the cumulative heat at 72 h is the highest for the slags with the highest CaO content, AA-C_6A_2 and AA-C_6A_1, suggesting that the reaction is continuing for a longer period when using slags with a higher CaO content. This was demonstrated by Siakati et al. [56], where the reaction extent of slags with a higher CaO/FeO ratio caught up and surpassed the reaction extent of the slags with a lower CaO/FeO ratio between 2 and 28 days. This might suggest AA-C_2A_1/$C_2A_1M_2$ would obtain lower strength while AA-C_6A_1 could gain strength for a longer period since many works suggested the cumulative heat agrees well with compressive strength [57-59]. The impact on the strength development is discussed in more detail in section 3.2.5.

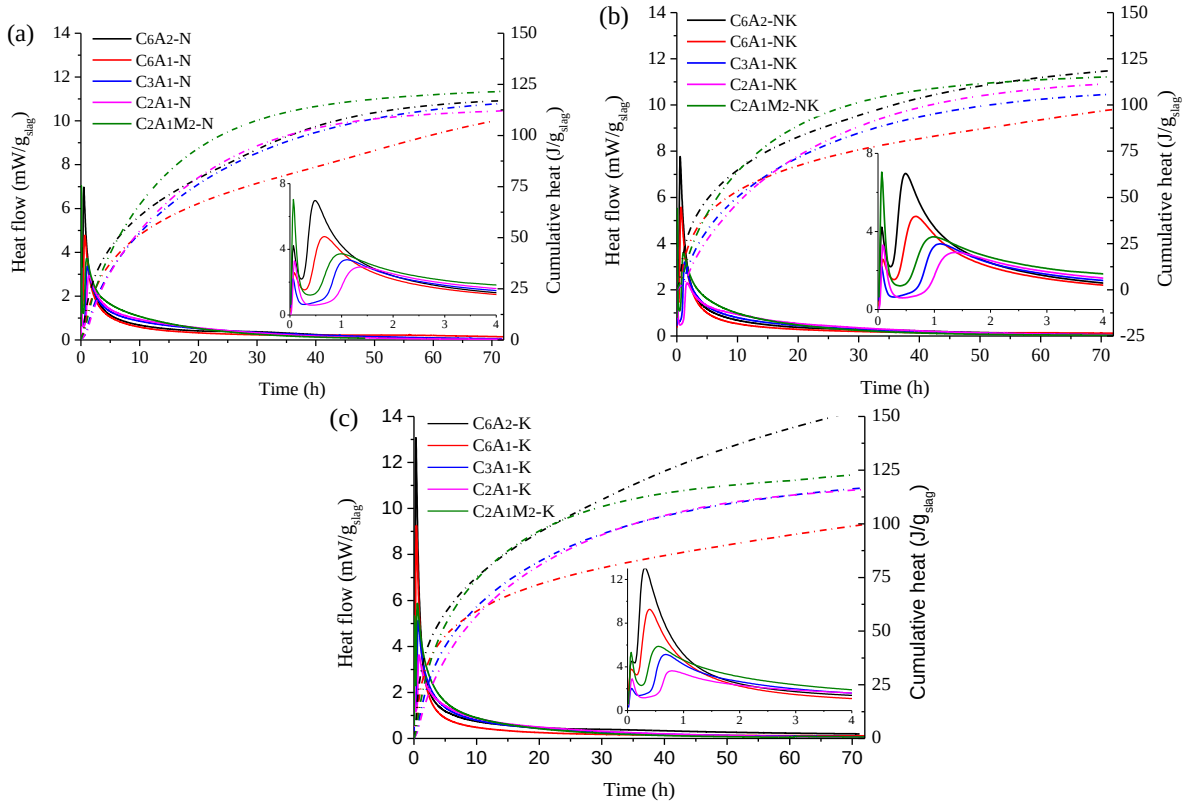

Fig. 2. Isothermal heat flow calorimetry of different slags at different activators for 3 days (a) -N solution; (b) -NK solution and (c) -K solution, Internal admix ampoules. T = 20.0 ± 0.2 °C

The effect of alkali activating solution on the heat flow during early hydration is illustrated in Fig 3. Nature and concentration of alkali solution ions can directly affect dissolution, precipitation, and thus the subsequent formation of reaction products as well as microstructural development of AA-NFMS [60]. The pH of three activators is usually one of the main factors for varied reaction kinetics of NFMS-based AAM and AAMs in general [2, 15]. However, due to the fixed SiO_2/M_2O molar ratio (M = Na or K), the pH (see Table 2) did not vary significantly among the three activators that were used in this study. As shown in Fig. 3 (a more detailed isothermal heat flow calorimetry is present in Appendix Fig. S.1), the peak flows for K-based AA-NFMS occurred earlier and obtained higher cumulative heat release than N- or NK-based AA-NFMS regardless of the slag chemistry. This is in line with earlier findings [50, 61]. Concerning the mixed NK activator, similar kinetics were observed as for the Na silicate

activated CaO-rich slags (16 wt%); however, at medium and low CaO contents (10 and 5 wt%), the reaction with the Na activator starts slightly earlier. The delay of the reaction when using a mixed Na+K solution seems to increase with the decreasing amount of CaO in the precursor. The reason for this is not clear enough from the data here. A more dedicated study would be needed.

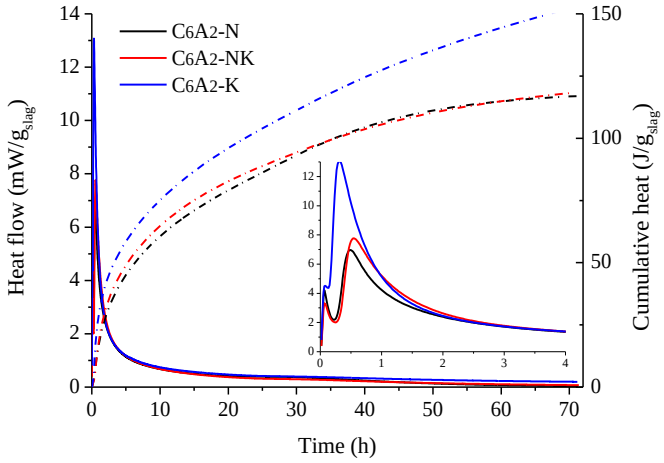

Fig. 3. Heat flow for first 72 hours of different alkali activating solutions for C_6A_2 slag. The heat flow for C_6A_1 slag, C_3A_1 slag, C_2A_1 slag and $C_2A_1M_2$ slag system are presented in the supplementary material (Fig. S.1)

There are many equations proposed to assess the materials' potential for alkaline activation. For NFMS, a quality coefficient (Eq. 1) was defined by Shi et al. [62].

$$K = \frac{CaO+MgO+Al_2O_3+Fe_2O_3+{}^1/_2FeO}{SiO_2+{}^1/_2FeO} \quad \text{Eq. 1}$$

From the XRF results (Table 1) and the oxidation state calculated (Table 3) above, the K value is presented in Table 4, indicating the higher Al_2O_3, CaO content and the replacement of CaO by MgO increases the potential of the NFMS to be alkali-activated.

Table 4 K-value of slag produced

	C_6A_2	C_6A_1	C_3A_1	C_2A_1	$C_2A_1M_2$
K-value	1.10	0.95	0.82	0.76	0.90

The second peak position in the figures of heat flow is an important parameter, as it could be roughly related to the setting time of AAM [63]. The relationship between the time of the second peak and the K-value, illustrated in Fig. 4, can be expressed as a linear correlation, but the linearity for the three activators is different. The mixed Na+K solution results in a lower R^2. For all five slags, C_6A_2 and C_6A_1 with high CaO contents slightly deviate from the general fit compared to other slags. But in general, K-value can still be correlated to the time of maximum heat flow peak as the R^2 is still relatively high. However, when correlating the K-value to 1 d or 3 d cumulative heat release, the R^2 is only around 0.1. According to [54, 62], a higher K value indicates a greater alkali activation potential. From the results here, it appears that applying the K-value as an indicator is not leading to the desired prediction as it focuses more on the time of the main peak and less on cumulative heat. Besides, the effort was also made to fit slag basicity (the ratio of (CaO% + MgO%) to SiO_2%) with cumulative heat. However, the R^2 of the linear fit (around 0.1 - 0.2) is very low.

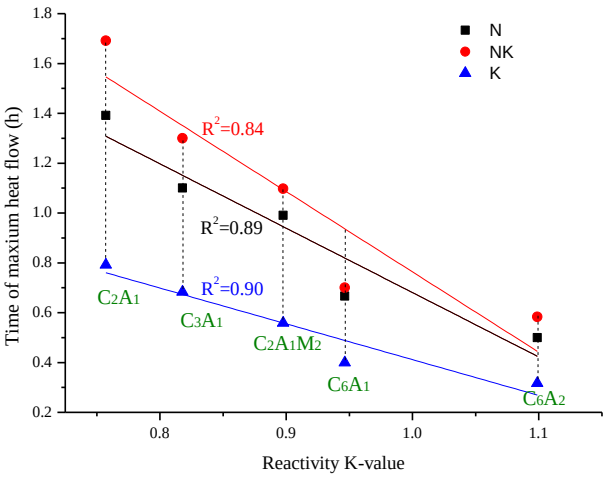

Fig. 4. The relation between reactivity K-value and the peak time for different AA-NFMS

3.2.2 Pore structure

Fig. 5 illustrates the relationship between the cumulative pore volume and pore sizes of a type of AA-NFMS with three different activators and the differential volume as a function of pore diameter is plotted in Fig. 6. Irrespective of the activating solution used, AA-C_6A_2 pastes

with higher Al/Si and Ca/Si ratios consistently exhibited the smallest total intruded pore volume and also the narrowest pore size distribution among the five types of slag chemistries studied. In contrast, the AA-$C_2A_1M_2$ paste with the presence of MgO showed the largest total volume with the broadest curve shape. Additionally, a higher Ca/Si ratio resulted in a lower total volume, from the comparison among AA-C_6A_1, C_3A_1 and C_2A, regardless of the nature of the activating solution. The impact of CaO content on total pore volume decreased as the K^+ concentration in the solution increased, as evidenced by the fact that the difference in total volume between C_6A_1 and C_2A_1 pastes in Na-activator (0.0072 mL/g) was approximately 28 times higher than that in K-solution (0.00025 mL/g).

The effect of activators on AA-NFMS was similar in C_6A_1 and C_6A_2, where the increasing K^+ in solution increased the total pore volume. However, in the medium CaO+MgO system (C_3A_1 and $C_2A_1M_2$), a Na-activation obtained the highest total pore volume and mixed NK-AAM showed the lowest total pore volume. This trend possibly implies the similar role of Mg and Ca in the studied cases. When the CaO concentration is decreased to C_2A_1, Na-activator results in a much larger total pore volume while K-activator leads to the lowest total pore volume, although the difference between the mixed Na+K solution and K-based solution is not highly detectable. The shift in the effect of activator cation on total pore volume suggests there is an interplay between precursors and activating solutions, leading to different reaction products per case, thus different microstructures. Further work is needed to shed light on the precise mechanisms.

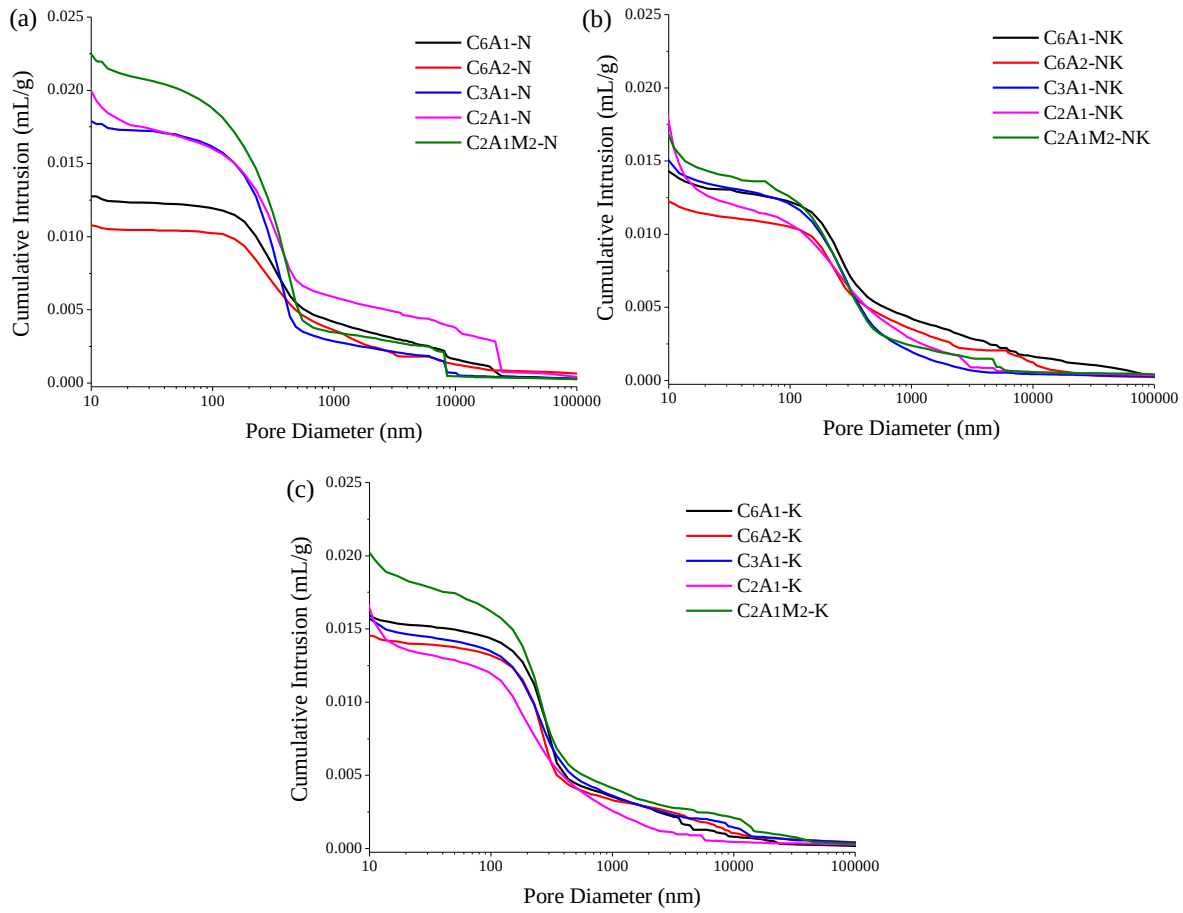

Fig. 5. Cumulative volume curve for AA-NFMS activated by (a) N solution; (b) NK solution; and (c) K solution

Pores in the 50 nm-200 nm range are formed starting from the early reaction stages when the main reaction products are produced [64]. Pores larger than 200 nm are present in the space between reaction products rather than in the products. The peak in the differential volume curve implies the critical (percolating) pore size in the AA-NFMS pastes [64]. The critical pore size is in the macropore region in the present study, which is quite larger than that of alkali-activated BFS in the mesopore region around 25 nm [65]. Fig. 6 indicates that the critical pore radius of the AA-NFMS is more closely associated with the activator rather than the slag chemistry. The pore size distribution in a pure Na-activated system is bimodal, with peaks centered at pore radius of 225 and 350 nm (the peak for 350 nm is more prominent). The first peak increases while the second peak decreases with increasing K+ concentration in the activating solution. The K-activated system presents a nearly single-peaked curve at a pore radius of approximately

225 nm. The lower critical pore radius of K-activation may explain why the K-activated NFMS system exhibits higher compressive strength despite the higher overall porosity, as observed in other studies [64, 66].

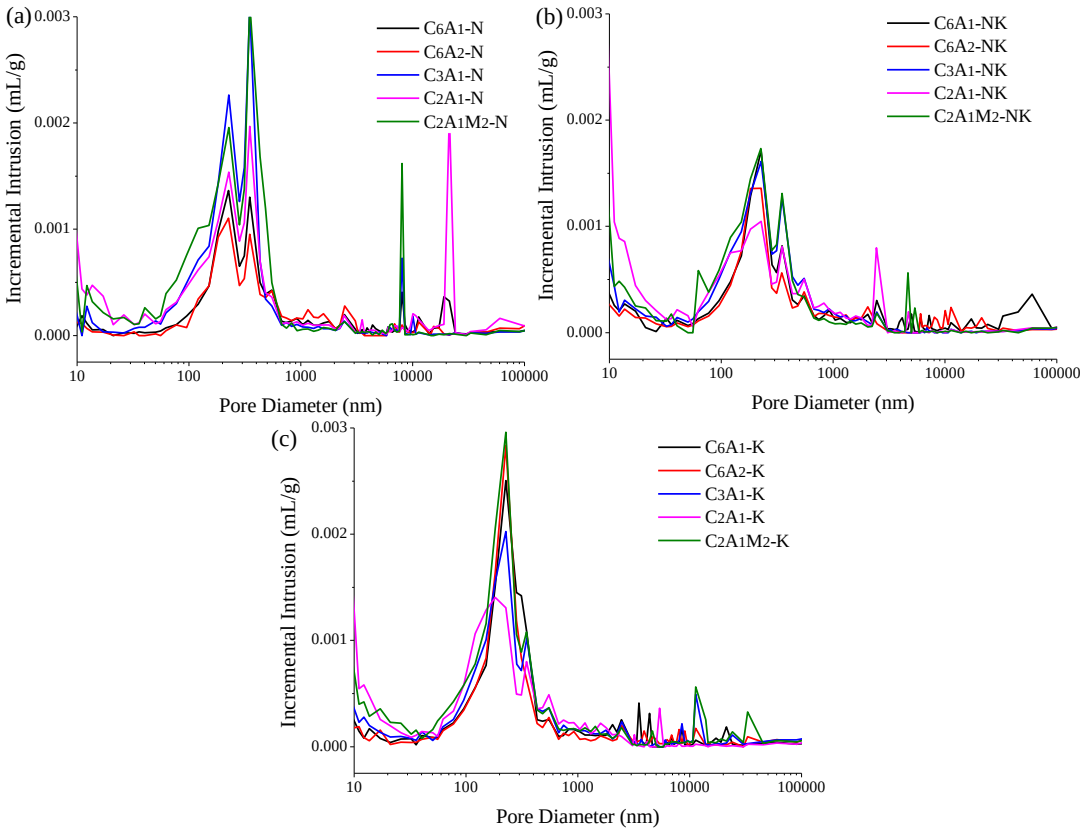

Fig. 6. Differential volume curve for (a) N- solution; (b) NK- solution: and (c) K-solution activated AAM pastes

Due to the intricate nature of the pore structure and the interplay between slag chemistry and the activating solution, **Fig. 7** was plotted on various pore ranges in the total pore volume of different NMFS and C_6A_2 samples subjected to different activating solutions. From the perspective of NMFS chemistry, it is noteworthy that despite achieving the lowest total porosity with higher Al/Si and Ca/Si ratios, a significant proportion of macro pores, particularly those exceeding 500 nm in size, was observed. Among the AA-NFMS with a medium Ca/Si ratio (specifically AA-C_3A_1), the smallest fraction of pores exceeding 500 nm was detected. Substituting Ca with Mg led to an increase in pore volume across all ranges. On the activating

solution side, an increase in K concentration resulted in elevated total porosity but a reduced proportion of larger pores (>500 nm). This observation underscores the significance of considering different pore diameters, as sometimes total porosity alone may not fully elucidate performance variations.

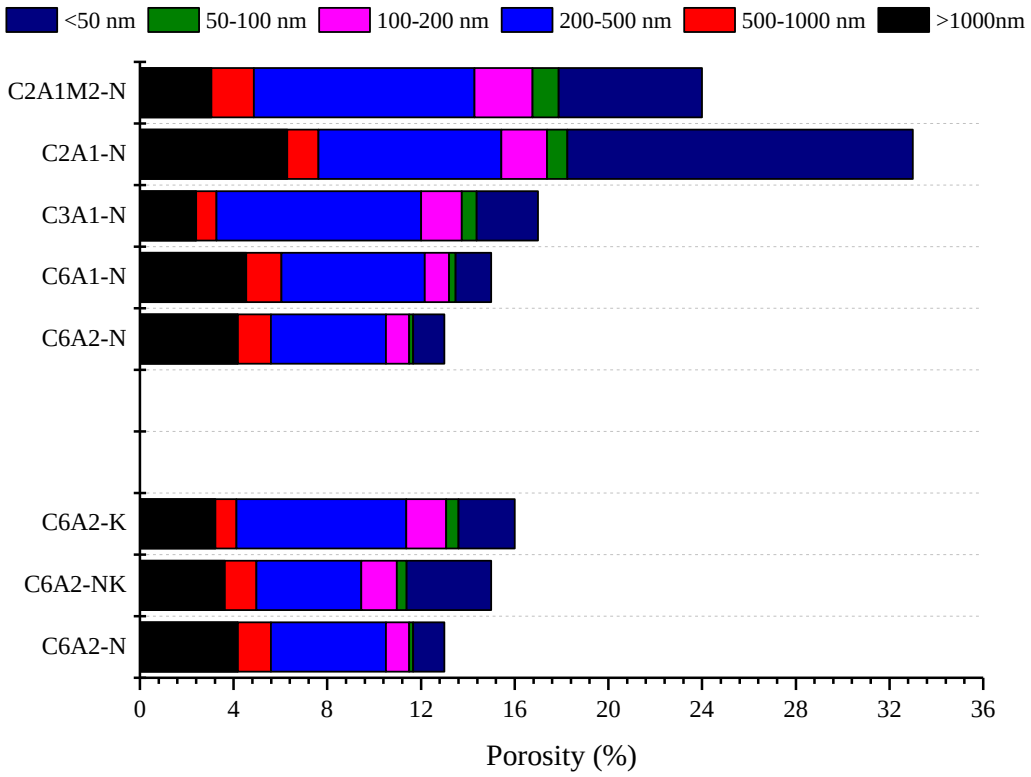

Fig. 7. Different pore diameter range in total porosity of different AA-NFMS under Na-activator and AA-C_6A_2 under different activating solution

3.2.5 Compressive strength

Fig. 8 illustrates the development of compressive strength in NFMS-AAM mortar at 3d, 7d, and 28d, which varied depending on the chemistry of the slags and activators employed. The AA-NFMS mortar made with C_6A_2 slag, characterized by the highest CaO and Al_2O_3 content, consistently demonstrated the highest compressive strength at all curing ages. Notably, the comparison between C_6A_1 and C_6A_2, with the same Ca/Si but different Al/Si ratios, showed that the compressive strength was consistently higher for C_6A_2, indicating the positive effect of Al_2O_3 on the system. This could be attributed to the higher Al/Si accelerating the reaction

[39], which is in line with the calorimetry data in section 3.2.1. In addition, the lower porosity (sections 3.2.2) of the reaction product of C_6A_2 also lead to higher mechanical performance.

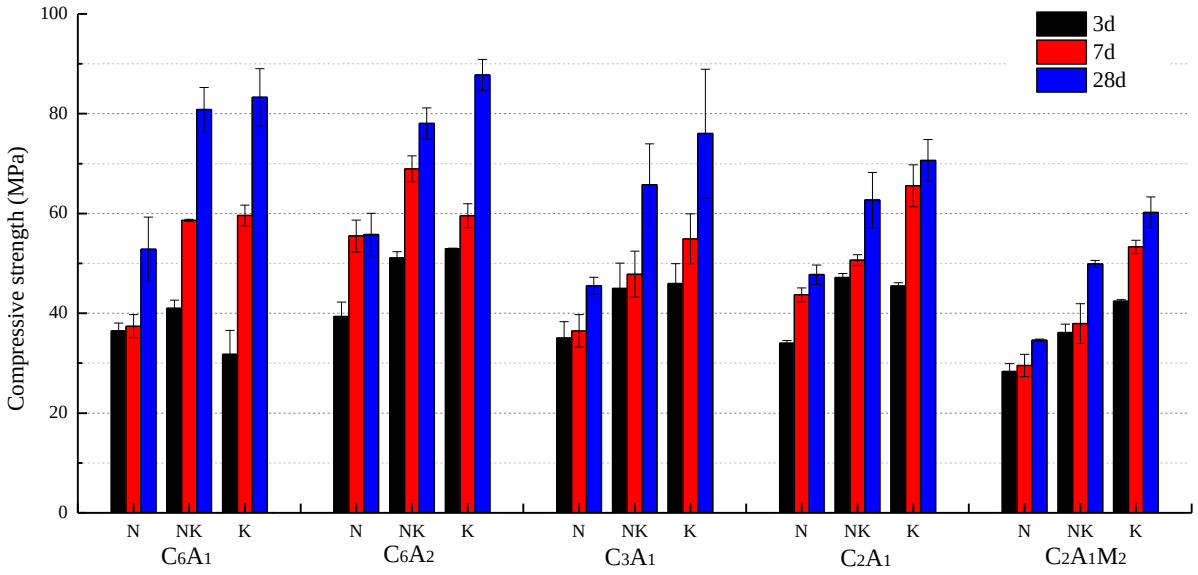

Fig. 8. Compressive strength development with time

The compressive strength of AA-NFMS mortars made from different Ca/Si exhibited distinct variations with curing time (AA-C_6A_1, C_3A_1 and C_2A_1). At an early age of 3 days, C_2A_1, with the lowest Ca/Si ratio, resulted in higher strength compared to C_6A_1. However, at a later age of 28 days, AA-C_6A_1 mortar demonstrated the highest compressive strength. For AAM mortars made from C_3A_1, with medium CaO content, the compressive strength was found to be intermediate between those of C_6A_1 and C_2A_1. The 28-day strength are consistent with the MIP results, where a lower porosity was detected for AA-NFMS mortars made from a higher Ca/Si NFMS, implying a positive correlation between compressive strength and denser microstructure. The role of Ca in this structure has not been determined with clarity. The lower early strength in the systems with a high amount of Ca suggests that it does not participate in strength-giving phases or hinders their formation in the early stages of the reaction. However, considering the importance of Ca for late strength, it is likely that a Ca-rich binding phase precipitates at a later age. In-situ studies on similar slags [26] explained the low early strength

of high CaO AA-NFMS: trioctahedral layers are part of the structure of alkali-activated non-ferrous slag. The incorporation of Ca distorts the trioctahedral layers and thus hinders the formation of these trioctahedral structures in the early stage. ^{57}Fe Mössbauer spectroscopy results indicated that a larger residual reaction extent was observed in a higher CaO AA-NFMS system [56] than in a low CaO counterpart, resulting in a higher compressive strength at a late age.

Regarding the effect of MgO, the replacement of CaO with MgO in $C_2A_1M_2$-AAM resulted in the lowest compressive strength at all ages of testing. Despite the lower strength of $C_2A_1M_2$-AAM, the absolute value is still reasonable. At an early age, the gap in strength between $C_2A_1M_2$-AAM and other activated slag systems is smaller than at a later age. This might be attributed to the improved reaction kinetics when MgO is added, as indicated in Section 3.2.1. Moreover, the cumulative heat release curve flattens faster for the MgO-containing slag (Fig. 2), suggesting that the reactions do not continue as much after 3 days, which explains why the strength difference is greater at a later age. The present findings also reinforce the significance of Ca in comparison to Mg in the enhancement of compressive strength in AA-NFMS.

For all five NFMS, K-based solution is the most effective activator regarding the compressive strength. Additionally, the curing time appears to have a greater impact on the compressive strength of K-based AA-NFMS, as evidenced by a substantial increase from 3 to 28 days, compared to Na-based AA-NFMS which exhibited a less intense increase. Irrespective of the slag composition, NK-activated system consistently demonstrated intermediate performance between Na- and K-based system. The superior performance of K-solution in terms of strength may be attributed to several factors. Firstly, the pH of K-solution is higher than the pH of Na-solution. The rate of dissolution depends on the pH of the starting solution [2], which is in line with the reactivity results above. The higher extent of dissolution, hence

more extensive binder formation, often leads to higher compressive strength [67]. Secondly, the ionic size of Na^+ is smaller than that of K^+. The larger ionic size of K^+ favors the formation of larger oligomers with which other ions prefer to bind, resulting in a higher compressive strength [67]. Thirdly, Na^+ is a moderately strongly hydrated cation while K^+ is a weakly hydrated cation [4], leading to a smaller amount of freely mobile water in Na-solution than in K-solution [68] and a difference in the size of the gel pores in the binder. Thus, a concentrated K-solution can flow with much less restriction, resulting in higher compressive strength. MIP results are supportive of this explanation. Finally, the activation of Fe-rich slag leads to an increase incoordination number of Fe by the presence of K during the dormant stage between the two heat flow peaks in calorimetry [26]. This shifts the local environment of Fe already towards that in the trioctahedral phyllosilicate, stimulating the formation of this reaction product. This might be an additional explanation for the observed strength increase. Due to the large amount of likely explanations, the observed effect is probably a combination of several of these phenomena.

The main objective of this research was to examine the impact of the chemical composition of the NFMS and activating solution on the properties of AA-NFMS. The variables considered in the study were limited to Ca/Si, Al/Si, (Ca+Mg)/Al from NFMS, and $K^+/(N^+{+}K^+)$ from the activating solution. An empirical model was developed using JMP software to assess the effects of these variables on the compressive strength of AA-NFMS. The model included all the relevant factors in the raw materials. The predicted strength values obtained from the refined model were compared with actual strength values and displayed in Fig. 9. The most significant terms in the model were identified as $K^+/(N^+{+}K^+)$, Ca/Si, and (Ca+Mg)/Si. Interestingly, the model indicated a negative effect of Mg on the 28-day strength, while Ca/Si had a positive effect. Surprisingly, higher Al/Si did not have a significant effect on the compressive strength in the studied cases. The fitted model had an R^2 value of 0.94 and a

root mean square error of 4.3 MPa. The predicted compressive strength values can be obtained from the following expression based on the refined model:

Compressive strength (28 day) = $38.1+28.3 \cdot K^+/(N^++K^+)+98.2 \cdot Ca/Si-62.3 \cdot (Ca+Mg)/Si$

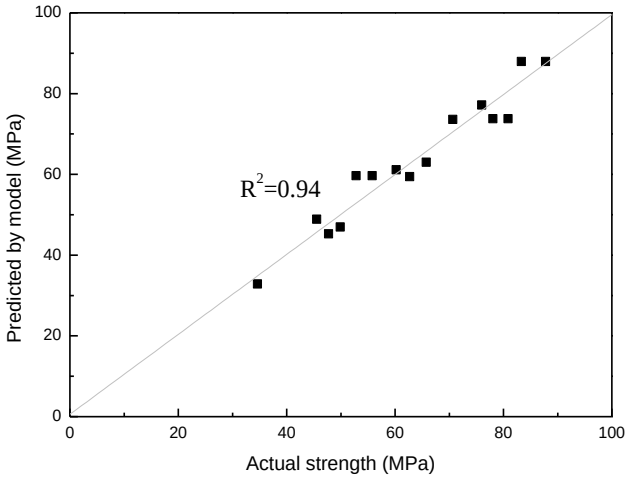

Fig. 9 Comparation of the actual and predicted compressive strength

In this study, the relationship between three characteristics of AA-NFMS, namely reaction kinetics, porosity, and compressive strength, were investigated. To assess the compressive strength performance of each AA-NFMS, a plot of cumulative heat vs compressive strength after 3-day curing was generated (Fig. 10). The low R^2 value of 0.41 suggests a weak correlation between these two parameters. This indicates that while cumulative heat may be a contributing factor in determining early strength, it is not the only determining factor [69]. Additionally, attempts were made to establish a correlation between the reactivity K-value calculated (Table 4) and compressive strength, but the R^2 value was found to be quite low (<0.4), highlighting that the K-value alone is insufficient to determine the alkaline activation potential of NFMS.

The relationship between pore characteristics and compressive strength is a reasonable avenue to explore, as demonstrated by previous studies [70, 71]. A previous study [64] found that pores larger than 200 nm have a stronger correlation with compressive strength than the

total pore volume in AAM systems. Herein, the pore volume at different scales was linearly fitted with compressive strength at 28 days. The resulting R^2 and slope are presented in Table 5. The inclusion of pores smaller than 200 nm resulted in a less steep slope, indicating that pores smaller than 200 nm might contribute to strength improvement. The R^2 value in Table 5 shows that the total pore volume is more closely related to compressive strength, but not solely due to pores larger than 200 nm (R^2 changed from 0.69 to 0.82 after including pores smaller than 200 nm). However, it is important to note that the relatively low R^2 value could be influenced by the limitations of the measurement methods used in this study.

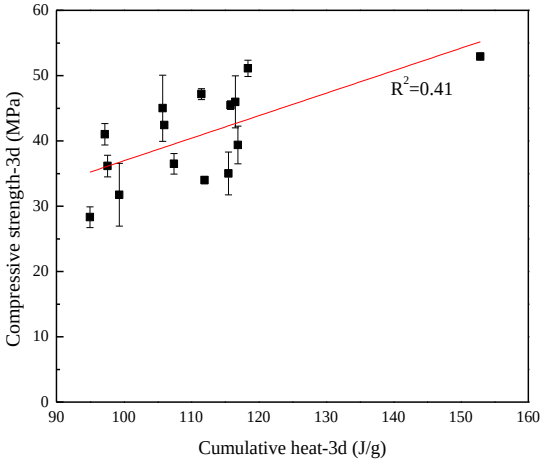

Fig. 10. Fitting the relationship between cumulative heat release and compressive strength at 3 days of curing

Table 5 Relationship between compressive strength at 28 d and the volume of pores at different scales from MIP measurement

	>1000nm	>500nm	>200nm	>100nm	>50nm	Total pore volume
R^2	0.04	0.35	0.69	0.74	0.76	0.82
Slope	-6.1	-7.8	-3.4	-3.2	-3.0	-3.4

3.2.6 Microstructure

In this section, we present additional microscopic characteristics of the AA-NFMS binder after a 28-day period, as determined through EPMA-WDS analysis. Fig. 11 depicts the

microstructure of AA-C_6A_2 under Na-activating solution; it is noteworthy that all AA-NFMS samples exhibited similar microstructural features.

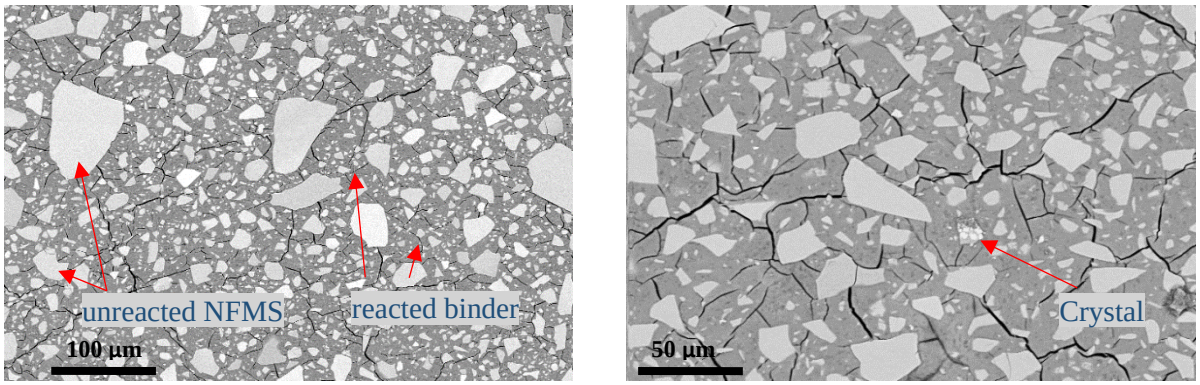

Fig. 11. Microstructure of AA-C_6A_2 under Na-activator

The microstructure analysis reveals that the solid binder comprises three distinct components: unreacted amorphous NFMS, unreacted crystal phases originating from NFMS (specifically, fayalite or forsterite and maghemite), and the amorphous reacted binder. To delve deeper into the chemical composition of these reaction products, we conducted point analysis at six different locations within the unreacted amorphous NFMS and six points within the reacted binder. The comprehensive results for all AA-NFMS samples are summarized in Table 6.

Table 6 Chemical composition from EPMA-WDX

	Unreacted NFMS					Reacted binder				
	Si	Al	Fe	Ca	Mg	Si	Al	Fe	Ca	Mg
C_6A_2	14.3±0.5	4.0±0.2	25.8±0.1	13±2	/	15.4±0.5	3.1±0.3	18.3±0.1	9.2±1.7	/
C_6A_1	15.1±0.4	3.6±0.1	27.3±1.0	10.3±0.3	/	15.0±0.8	3.4±0.1	18.1±0.9	6.9±2.0	/
C_3A_1	14.6±1.6	3.2±0.3	29.9±3.5	6.8±0.8	/	16.0±0.6	2.4±0.3	18.4±1.0	4.7±0.7	/
C_2A_1	18.1±1.3	3.8±0.5	26.7±0.9	5.5±0.6	/	19.4±1.6	2.9±0.6	19.9±0.5	3.8±0.1	/
$C_2A_1M_2$	17.2±1.6	3.4±0.3	28.8±2.0	4.7±0.2	1.8±0.1	16.7±0.5	2.3±0.2	20.2±0.4	4.6±0.2	1.1±0.2

In comparison to XRF data of NFMS, the composition of the amorphous NFMS exhibits a lower Fe content, owing to some Fe presence within the crystal phases. The composition of the reacted binder and the amorphous slag are notably similar, with the exception that the reacted binder displays an elevated Si content due to the addition of the Na-activator.

Consequently, the concentrations of other elements such as Fe, Al, and Ca are correspondingly lower in the reacted binder. It is imperative to recognize that the measured total composition of the reacted binder appears lower due to the water content and the presence of pores formed within the reaction products.

Fig. 12 offers a visual representation of the composition of these points in terms of their (Ca+Mg)/Si and Al/Si molar ratios. As before noticed, the reacted binder exhibits lower Ca/Si and Al/Si ratios than the NFMS, primarily due to the Si introduced from the activating solution. The linear fitting of (Ca+Mg)/Si and Al/Si ratios for the slag and binder showcases decent alignment, characterized by identical linear fitting slopes, except in the case of $C_2A_1M_2$, where MgO is present in the slag. Previous research has suggested the potential combination of Mg with Al, forming layered double hydroxides of the hydrotalcite group. The higher Ca/Al ratio observed in the amorphous reacted binder of AA-$C_2A_1M_2$, in comparison to the $C_2A_1M_2$ slag, could indicate the presence of this phase. Nevertheless, the limited quantity or small grain size of this phase precludes its detection through XRD or EPMA analysis. Therefore, further dedicated research is required to analysis the formation of the hydrotalcite.

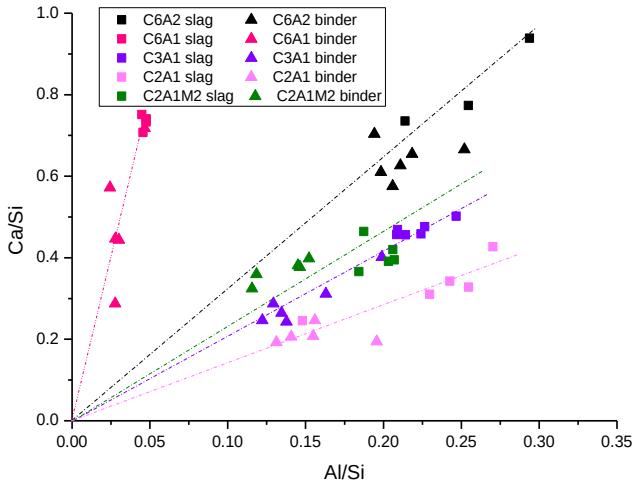

Fig. 12. EPMA-WDS point analysis of AA-NFMS under Na-activator in terms of Al/Si and Ca/Si molar ratios.

4. Conclusion

Five synthetic NFMS in the FeO_x-SiO_2-Al_2O_3-CaO-MgO system with the same FeO_x/SiO_2 molar ratio were used to produce AA-NFMS under three different activators. The following conclusion can be drawn:

(1) The dissolution and reaction of slags can be accelerated by increasing Al_2O_3 content in the slag. Higher CaO concentration hindered reactions at the beginning but the reaction continued for a longer period. In addition, the partial replacement of CaO by MgO ($C_2A_1M_2$) in the AA-NFMS system led to faster kinetics but the reactions reaches the plateau earlier.

(2) The reaction products of investigated AA-NFMS are amorphous and filled with pores. Both the chemical composition of slag and the nature of the solution affect the pore size distribution as deduced from MIP tests. The higher level of Al_2O_3 and CaO concentration favors a smaller total pore volume, while the presence of MgO increased the pore volume.

(3) For the investigated AA-NFMS, the K-based activating solution was the most effective activator compared to Na-based and mixed Na/K solutions regarding the reactivity and compressive strength of the resulting mortars. Samples that are activated by K-activator exhibited a higher porosity but smaller pores compared to Na-activation.

(4) A higher level of Al_2O_3 in the slag increases the compressive strength at 3, 7, and 28 d. CaO content plays a complex role in compressive strength, as increasing CaO decreases the early strength but improves the late compressive strength. The replacement of CaO by MgO decreases the strength slightly (C_3A_1 vs $C_2A_1M_2$).

(5) The effect of raw materials on compressive strength was investigated using the JMP model, revealing that $K^+/(N^+{+}K^+)$, Ca/Si, and (Ca+Mg)/Si were the most significant terms. Furthermore, the correlation analysis indicated that porosity had a stronger association with compressive strength than reaction kinetics.

The results in this work highlighted that both slag and activator chemistry have a rather profound impact on the reactivity, pore structure and mechanical performance of the AA-NFMS system. The impact of these factors is expected to be notable also in the long-term performance (durability), and this will be assessed in a separate, dedicated study.

Acknowledgements

The authors acknowledge the financial support of SIM-Flanders within the framework of the MaRes program for project HBC.2018.0479.

Reference

[1] P.J.M. Monteiro, S.A. Miller, A. Horvath, Towards sustainable concrete, Nat Mater 16(7) (2017) 698-699.

[2] J.L. Provis, Alkali-activated materials, Cement and Concrete Research 114 (2018) 40-48.

[3] V. Ponomar, J. Yliniemi, E. Adesanya, K. Ohenoja, M. Illikainen, An overview of the utilisation of Fe-rich residues in alkali-activated binders: Mechanical properties and state of iron, Journal of Cleaner Production 330 (2022).

[4] P.N. Lemougna, K.-t. Wang, Q. Tang, U.C. Melo, X.-m. Cui, Recent developments on inorganic polymers synthesis and applications, Ceramics International 42(14) (2016) 15142-15159.

[5] P. Duxson, J.L. Provis, Designing Precursors for Geopolymer Cements, Journal of the American Ceramic Society 91(12) (2008) 3864-3869.

[6] A. Peys, V. Isteri, J. Yliniemi, A.S. Yorkshire, P.N. Lemougna, C. Utton, J.L. Provis, R. Snellings, T. Hanein, Sustainable iron-rich cements: Raw material sources and binder types, Cement and Concrete Research 157 (2022) 106834.

[7] G. Habert, S.A. Miller, V.M. John, J.L. Provis, A. Favier, A. Horvath, K.L. Scrivener, Environmental impacts and decarbonization strategies in the cement and concrete industries, Nature Reviews Earth & Environment 1(11) (2020) 559-573.

[8] K.K. Ramagiri, A. Kar, Environmental impact assessment of alkali-activated mortar with waste precursors and activators, Journal of Building Engineering 44 (2021) 103391.

[9] I. Faridmehr, M.L. Nehdi, M. Nikoo, G.F. Huseien, T. Ozbakkaloglu, Life-Cycle Assessment of Alkali-Activated Materials Incorporating Industrial Byproducts, Materials 14(9) (2021) 2401.

[10] I. Ramón-Álvarez, E. Batuecas, S. Sánchez-Delgado, M. Torres-Carrasco, Mechanical performance after high-temperature exposure and Life Cycle Assessment (LCA) according to unit of stored energy of alternative mortars to Portland cement, Construction and Building Materials 365 (2023) 130082.

[11] B.C. Mendes, L.G. Pedroti, C.M.F. Vieira, M. Marvila, A.R.G. Azevedo, J.M. Franco de Carvalho, J.C.L. Ribeiro, Application of eco-friendly alternative activators in alkali-activated materials: A review, Journal of Building Engineering 35 (2021).

[12] B. Sun, G. Ye, G. de Schutter, A review: Reaction mechanism and strength of slag and fly ash-based alkali-activated materials, Construction and Building Materials 326 (2022).

[13] J.L. Provis, A. Palomo, C. Shi, Advances in understanding alkali-activated materials, Cement and Concrete Research 78 (2015) 110-125.

[14] A. Peys, A.P. Douvalis, V. Hallet, H. Rahier, B. Blanpain, Y. Pontikes, Inorganic Polymers From CaO-FeOx-SiO2 Slag: The Start of Oxidation of Fe and the Formation of a Mixed Valence Binder, Frontiers in Materials 6 (2019).

[15] J. Van De Sande, A. Peys, T. Hertel, H. Rahier, Y. Pontikes, Upcycling of non-ferrous metallurgy slags: Identifying the most reactive slag for inorganic polymer construction materials, Resources, Conservation and Recycling 154 (2020) 104627.

[16] J. Zhang, C. Shi, Z. Zhang, Z. Ou, Durability of alkali-activated materials in aggressive environments: A review on recent studies, Construction and Building Materials 152 (2017) 598-613.

[17] N.M. Piatak, M.B. Parsons, R.R. Seal, Characteristics and environmental aspects of slag: A review, Applied Geochemistry 57 (2015) 236-266.

[18] M. Khorasanipour, E. Esmaeilzadeh, Environmental characterization of Sarcheshmeh Cu-smelting slag, Kerman, Iran: Application of geochemistry, mineralogy and single extraction methods, Journal of Geochemical Exploration 166 (2016) 1-17.

[19] J. Singh, S.P. Singh, Synthesis of alkali-activated binder at ambient temperature using copper slag as precursor, Materials Letters 262 (2020) 127169.

[20] P.P. Sivakumar, Mix development and performance of concrete with treated slag from copper production as cement and sand replacement, Faculty of Engineering and Architecture, Ghent University, Ghent, Belgium, 2022.

[21] S. Onisei, K. Lesage, B. Blanpain, Y. Pontikes, L. Struble, Early Age Microstructural Transformations of an Inorganic Polymer Made of Fayalite Slag, Journal of the American Ceramic Society 98(7) (2015) 2269-2277.

[22] Y. Pontikes, L. Machiels, S. Onisei, L. Pandelaers, D. Geysen, P.T. Jones, B. Blanpain, Slags with a high Al and Fe content as precursors for inorganic polymers, Applied Clay Science 73 (2013) 93-102.

[23] C. Siakati, A.P. Douvalis, P. Ziogas, A. Peys, Y. Pontikes, Impact of the solidification path of FeO_x–SiO_2 slags on the resultant inorganic polymers, Journal of the American Ceramic Society 103(3) (2019) 2173-2184.

[24] L. Stefanini, S. Ghorbani, G. De Schutter, S. Matthys, B. Walkley, J.L. Provis, Evaluation of copper slag and stainless steel slag as replacements for blast furnace slag in binary and ternary alkali-activated cements, Journal of Materials Science 58(31) (2023) 12537-12558.

[25] C. Siakati, A.P. Douvalis, A. Peys, Y. Pontikes, Binary, ternary and quaternary Fe-rich slags: Influence of Fe and Si substitution by Ca and Al on the atomic structure and reactivity, Conference: 6th International Slag Valorisation Symposium (2019).

[26] A. Peys, C.E. White, H. Rahier, B. Blanpain, Y. Pontikes, Alkali-activation of CaO-FeOx-SiO2 slag: Formation mechanism from in-situ X-ray total scattering, Cement and Concrete Research 122 (2019) 179-188.

[27] C. Siakati, R. Macchieraldo, B. Kirchner, F. Tielens, A. Peys, D. Seveno, Y. Pontikes, Unraveling the nano-structure of a glassy CaO-FeO-SiO2 slag by molecular dynamics simulations, Journal of Non-Crystalline Solids 528 (2020).

[28] A. Peys, A.P. Douvalis, C. Siakati, H. Rahier, B. Blanpain, Y. Pontikes, The influence of air and temperature on the reaction mechanism and molecular structure of Fe-silicate inorganic polymers, Journal of Non-Crystalline Solids 526 (2019).

[29] V. Ponomar, E. Adesanya, K. Ohenoja, M. Illikainen, High-temperature performance of slag-based Fe-rich alkali-activated materials, Cement and Concrete Research 161 (2022) 106960.

[30] V. Hallet, M.T. Pedersen, B. Lothenbach, F. Winnefeld, N. De Belie, Y. Pontikes, Hydration of blended cement with high volume iron-rich slag from non-ferrous metallurgy, Cement and Concrete Research 151 (2022) 106624.

[31] V. Hallet, M.T. Pedersen, B. Lothenbach, F. Winnefeld, L. Eykens, N. De Belie, Y. Pontikes, The hydration of ternary blended cements with Fe-rich slag from non-ferrous metallurgy and limestone, Cement and Concrete Research 169 (2023) 107155.

[32] J. Astoveza, R. Trauchessec, S. Migot-Choux, R. Soth, Y. Pontikes, Iron-rich slag addition in ternary binders of Portland cement, aluminate cement and calcium sulfate, Cement and Concrete Research 153 (2022) 106689.

[33] T. Hertel, Y. Pontikes, Geopolymers, inorganic polymers, alkali-activated materials and hybrid binders from bauxite residue (red mud) – Putting things in perspective, Journal of Cleaner Production 258 (2020) 120610.

[34] M. Giels, T. Hertel, K. Gijbels, W. Schroeyers, Y. Pontikes, High performance mortars from vitrified bauxite residue; the quest for the optimal chemistry and processing conditions, Cement and Concrete Research 155 (2022) 106739.

[35] Y. Liu, D. Kumar, W. Zhu, Z. Chen, K.H. Lim, Y.L. Lai, Z. Hu, E.-H. Yang, Utilization of coarse non-ferrous fraction of incineration bottom ash as aerating agent in autoclaved aerated concrete, Construction and Building Materials 375 (2023) 130906.

[36] B. Walkley, R. San Nicolas, M.-A. Sani, S.A. Bernal, J.S.J. van Deventer, J.L. Provis, Structural evolution of synthetic alkali-activated CaO-MgO-Na 2 O-Al 2 O 3 -SiO 2 materials is influenced by Mg content, Cement and Concrete Research 99 (2017) 155-171.

[37] M. Giels, T. Hertel, Y. Pontikes, Alkali-activation of VITRIFIED Bauxite residue: The effect of MgO, Proceedings of the 6th international Slag Valorisation Symposium, Procopia, 2019, pp. 415-418.

[38] M. Ben Haha, B. Lothenbach, G. Le Saout, F. Winnefeld, Influence of slag chemistry on the hydration of alkali-activated blast-furnace slag — Part I: Effect of MgO, Cement and Concrete Research 41(9) (2011) 955-963.

[39] M. Ben Haha, B. Lothenbach, G. Le Saout, F. Winnefeld, Influence of slag chemistry on the hydration of alkali-activated blast-furnace slag — Part II: Effect of Al2O3, Cement and Concrete Research 42(1) (2012) 74-83.

[40] D.A. Lange, H. M.Jennings, S. P.Shah, Image analysis techniques for characterization of pore strucutre of cement-based materials, Cement and Concrete Research 24 (1994) 13.

[41] P. Steins, A. Poulesquen, F. Frizon, O. Diat, J. Jestin, J. Causse, D. Lambertin, S. Rossignol, Effect of aging and alkali activator on the porous structure of a geopolymer, Journal of Applied Crystallography 47(1) (2014) 316-324.

[42] K. Yang, C.E. White, Multiscale pore structure determination of cement paste via simulation and experiment: The case of alkali-activated metakaolin, Cement and Concrete Research 137 (2020) 106212.

[43] A.M. Rashad, Y. Bai, P.A.M. Basheer, N.C. Collier, N.B. Milestone, Chemical and mechanical stability of sodium sulfate activated slag after exposure to elevated temperature, Cement and Concrete Research 42(2) (2012) 333-343.

[44] M.M. Hossain, M.R. Karim, M.M. A Elahi, M.F. Mohd Zain, Water absorption and sorptivity of alkali-activated ternary blended composite binder, Journal of Building Engineering 31 (2020) 101370.

[45] S. Park, B. Lothenbach, J.G. Jang, H.-K. Kim, N. Lee, Thermodynamic Modeling and Experimental Study of Carbonation of Alkali-Activated Slag Cements, ACS Sustainable Chemistry & Engineering 11(10) (2023) 4049-4063.

[46] T. Bakharev, Durability of geopolymer materials in sodium and magnesium sulfate solutions, Cement and Concrete Research 35(6) (2005) 1233-1246.

[47] P. Duxson, J.L. Provis, G.C. Lukey, S.W. Mallicoat, W.M. Kriven, J.S.J. van Deventer, Understanding the relationship between geopolymer composition, microstructure and mechanical properties, Colloids and Surfaces A: Physicochemical and Engineering Aspects 269(1) (2005) 47-58.

[48] A. Peys, C.E. White, D. Olds, H. Rahier, B. Blanpain, Y. Pontikes, Molecular structure of CaO–FeOx–SiO2glassy slags and resultant inorganic polymer binders, Journal of the American Ceramic Society 101(12) (2018) 5846-5857.

[49] B.O. Mysen, D. Virgo, E.-R. Neumann, F.A. Seifert, Redox equilibria and the structural states of ferric and ferrous iron in melts in the system CaO-MgGAl 2 O 3-, SiO 2-FeO : relationships between redox equilibria , melt structure and liquidus phase equilibria, 2007.

[50] V. Hallet, A. Peys, A. Katsiki, H. Rahier, S. Onisei, Y. Pontikes, The influence of activating solution on the kinetics and compressive strength of an iron-rich slag paste, 5th International Slag Valorisation Symposium: From Fundamentals to Applications (2017) 4.

[51] K. Scrivener, R. Snellings, B. Lothenbach, A Practical Guide to Microstructural Analysis of Cementitious Materials., CRC Press (2017).

[52] S. Simon, G.J.G. Gluth, A. Peys, S. Onisei, D. Banerjee, Y. Pontikes, The fate of iron during the alkali-activation of synthetic (CaO-)FeOx-SiO2 slags: An Fe K-edge XANES study, Journal of the American Ceramic Society 101(5) (2018) 2107-2118.

[53] S.A. Bernal, R. San Nicolas, R.J. Myers, R. Mejía de Gutiérrez, F. Puertas, J.S.J. van Deventer, J.L. Provis, MgO content of slag controls phase evolution and structural changes induced by accelerated carbonation in alkali-activated binders, Cement and Concrete Research 57 (2014) 33-43.

[54] J.L. Provis, J.S.J. Van Deventer, Alkali-activated materials, (2013).

[55] Y. Ma, X. Yang, J. Hu, Z. Zhang, H. Wang, Accurate determination of the "time-zero" of autogenous shrinkage in alkali-activated fly ash/slag system, Composites Part B: Engineering 177 (2019) 107367.

[56] C. Siakati, A.P. Douvalis, V. Hallet, A. Peys, Y. Pontikes, Influence of CaO/FeO ratio on the formation mechanism and properties of alkali-activated Fe-rich slags, Cement and Concrete Research 146 (2021).

[57] S. Ramanathan, P. Suraneni, Y. Wang, H. Shan, A. Hajibabaee, J. Weiss, Combining Reactivity Test, Isothermal Calorimetry, and Compressive Strength Measurements to Study Conventional and Alternative Supplementary Cementitious Materials, Springer International Publishing, Cham, 2020, pp. 445-454.

[58] R. Tänzer, A. Buchwald, D. Stephan, Effect of slag chemistry on the hydration of alkali-activated blast-furnace slag, Materials and Structures 48(3) (2015) 629-641.

[59] J. Yliniemi, B. Walkley, J.L. Provis, P. Kinnunen, M. Illikainen, Influence of activator type on reaction kinetics, setting time, and compressive strength of alkali-activated mineral wools, Journal of Thermal Analysis and Calorimetry 144(4) (2021) 1129-1138.

[60] J. Osio-Norgaard, J.P. Gevaudan, W.V. Srubar, A review of chloride transport in alkali-activated cement paste, mortar, and concrete, Construction and Building Materials 186 (2018) 191-206.

[61] M. Salman, O. Cizer, Y. Pontikes, R. Snellings, L. Vandewalle, B. Blanpain, K. Van Balen, Cementitious binders from activated stainless steel refining slag and the effect of alkali solutions, J Hazard Mater 286 (2015) 211-9.

[62] C. Shi, D. Roy, P. Krivenko, Alkali-Activated Cements and Concretes (1st ed.). CRC Press., (2003).

[63] H. Rahier, J. Wastiels, M. Biesemans, R. Willlem, G. Van Assche, B. Van Mele, Reaction mechanism, kinetics and high temperature transformations of geopolymers, Journal of Materials Science 42(9) (2006) 2982-2996.

[64] Z. Peng, K. Vance, A. Dakhane, R. Marzke, N. Neithalath, Microstructural and 29Si MAS NMR spectroscopic evaluations of alkali cationic effects on fly ash activation, Cement and Concrete Composites 57 (2015) 34-43.

[65] F. Collins, J. Sanjayan, Effect of pore size distribution on drying shrinkage of alkali-activated slag concrete, Cement and Concrete Research 30 (2000).

[66] J. Zhu, R. Zhang, Y. Zhang, F. He, The fractal characteristics of pore size distribution in cement-based materials and its effect on gas permeability, Sci Rep 9(1) (2019) 17191.

[67] J.S.J.V.D. Hua Xu, <The geopolymerisation of alumino-silicate minerals.pdf>, Int. J. Miner. Process. 59 (2000) 247–266.

[68] J.L. Provis, S.A. Bernal, Geopolymers and Related Alkali-Activated Materials, Annual Review of Materials Research 44(1) (2014) 299-327.

[69] S.A. Bernal, J.L. Provis, R.J. Myers, R. San Nicolas, J.S.J. van Deventer, Role of carbonates in the chemical evolution of sodium carbonate-activated slag binders, Materials and Structures 48(3) (2014) 517-529.

[70] C. Lian, Y. Zhuge, S. Beecham, The relationship between porosity and strength for porous concrete, Construction and Building Materials 25(11) (2011) 4294-4298.

[71] I. Odler, M. Rößler, Investigations on the relationship between porosity, structure and strength of hydrated Portland cement pastes. II. Effect of pore structure and of degree of hydration, Cement and Concrete Research 15(3) (1985) 401-410.